crystals

Article

Highly Efficient Orange-Red Emission in Sm^{3+}-Doped Yttrium Gallium Garnet Single Crystal

Huiting Zhang [1], Zhonghua Zhu [1], Shengdi Ta [1], Ninghan Zeng [1], Limin Wu [1], Wenxia Wu [1], Peng Zhang [1], Shoulei Xu [1,2], Bernard Albert Goodman [1] and Wen Deng [1,2,*]

[1] School of Physical Science and Technology, Guangxi University, 100 East Daxue Road, Nanning 530004, China; 2107301175@st.gxu.edu.cn (H.Z.); 2107301199@st.gxu.edu.cn (Z.Z.); 2007301125@st.gxu.edu.cn (S.T.); 2107301006@st.gxu.edu.cn (N.Z.); 2107301147@st.gxu.edu.cn (L.W.); 1907301088@st.gxu.edu.cn (W.W.); 2007301183@st.gxu.edu.cn (P.Z.); xsl@gxu.edu.cn (S.X.); bernard_a_goodman@outlook.com (B.A.G.)

[2] State Key Laboratory of Featured Metal Materials and Life-Cycle Safety for Composite Structures, Nanning 530004, China

* Correspondence: wdeng@gxu.edu.cn

Abstract: High-quality single crystals with empirical composition $Y_{2\cdot96}Sm_{0\cdot04}Ga_5O_{12}$ (YGG: Sm^{3+}) were successfully prepared by the optical floating zone method for the first time and compared with related single crystals of $Y_{2\cdot96}Sm_{0\cdot04}Al_5O_{12}$ (YAG: Sm^{3+}). With both crystals, XRD showed that Sm^{3+} entered the cubic-phase structure. Optical absorption spectra produced a series of peaks from Sm^{3+} in the 250 nm to 550 nm range, and photoluminescence excitation (PLE) spectra detected at 613 nm showed strong excitation peaks at 407 nm and 468 nm. A strong emission peak at 611 nm (orange-red light) was observed in the photoluminescence (PL) spectra under excitations at both 407 and 468 nm, respectively, but it was much brighter under excitation at 407 nm. Furthermore, with both emission spectra, the peaks from the YGG: Sm^{3+} crystal were significantly more intense than those from the YAG: Sm^{3+} crystal, and both experienced a blue shift. In addition, under excitation at 407 nm, the color purity of the emitted orange-red light of YGG: Sm^{3+} was higher than that of the YAG: Sm^{3+} crystal, and the fluorescence lifetime for the ${}^4G_{5/2} \rightarrow {}^6H_{7/2}$ transition of YGG: Sm^{3+} was longer than that of the YAG: Sm^{3+} crystal. The optical properties of the YGG: Sm^{3+} crystal are better than those of the YAG: Sm^{3+} crystal.

Keywords: optical properties; Sm^{3+}-doped yttrium gallium garnet single crystals; optical floating zone method; orange-red emission materials

check for updates

Citation: Zhang, H.; Zhu, Z.; Ta, S.; Zeng, N.; Wu, L.; Wu, W.; Zhang, P.; Xu, S.; Goodman, B.A.; Deng, W. Highly Efficient Orange-Red Emission in Sm^{3+}-Doped Yttrium Gallium Garnet Single Crystal. *Crystals* **2023**, *13*, 1273. https://doi.org/10.3390/cryst13081273

Academic Editor: Ana M. Garcia-Deibe

Received: 30 July 2023
Revised: 9 August 2023
Accepted: 14 August 2023
Published: 18 August 2023

1. Introduction

Rare-earth-based luminescent materials have been widely studied for their excellent spectral properties, which include a high and adjustable luminescence, long fluorescence lifetime, and large Stokes shift [1,2]. Consequently, they have extensive uses in light-emitting diodes (LEDs), lasers, optical temperature sensors, optical communications, display panels, luminescence dosimeters, and biomedical diagnostics [3–6]. Nevertheless, considerable efforts are still being employed to improve the luminescence properties of such rare-earth-doped materials [7–9], and the color, intensity, and luminescence efficiency have been shown to strongly depend on the structure and composition of the luminescent center [8,10]. Furthermore, the crystal structure, ionic radius, luminescence efficiency, refractive index, and phonon energy are key factors in determining the suitability of hosts and dopants, and the usefulness of certain fluorescent materials is dependent on their unique compositions [11].

Oxides with a garnet structure are commonly used as hosts for rare-earth-doped luminescent materials, and commercial w-LED lamps are currently manufactured using a combination of YAG: (Ce^{3+}, Sm^{3+}) yellow and red phosphors [12,13]. However, there are manufacturing problems associated with the use of these materials, including an uneven dispersion of the phosphor particles, short lifetimes, and low thermal conductivity [13,14], and the search for new white LED fluorescent materials to replace traditional phosphors is an ongoing research topic [15,16]. Furthermore, although rare-earth-doped materials with a garnet structure have desirable properties, including high excitation and emission efficiency, uniform distributions of rare-earth ions, a physical and chemical stability, long life, and high thermal conductivity, which are suitable for use in high-quality w-LEDs [17], there is still a need to improve the color temperature and color purity of white light by obtaining more efficient red light emission [18,19]. Thus, the fact that Sm^{3+} can achieve efficient orange-red light emission as a result of high absorptions near 404 nm and 468 nm, and thus can be efficiently excited by InGaN-based blue or UV LEDs, indicates that Sm^{3+}-doped materials with a garnet structure could be appropriate for use in w-LED devices [18,20].

Recently, it has been reported that Eu^{3+} transitions in Eu^{3+}-doped YAG are enhanced by replacing the Al^{3+} with Ga^{3+} [21] and that the luminescence intensity in YGG crystals is stronger than in YAG [22]. Furthermore, doping of YGG with other rare-earth ions, such as Er^{3+} and Tm^{3+}, has also been described [23], but we are unaware of any reports on the fluorescence properties of Sm^{3+}-doped YGG crystals.

Compared with ceramics and polycrystalline materials, single crystals have a greater atomic uniformity, better mechanical properties, and a higher electrochemical and thermal stability [24,25]. Furthermore, garnet single crystals are transparent materials, have a low defect density, no grain boundaries that affect the properties of ceramics, and negligible surface effects that influence the properties of powders. As a consequence, they have high photoluminescence quantum yields [26,27], and their use can improve the power and lifetime of w-LEDs [18,28]. Additionally, although traditional high-temperature methods for obtaining single crystals often suffer from contamination from crucibles, this problem is overcome with the optical floating zone method [29,30], which does not require a crucible and has a rapid crystal production cycle [31], which is advantageous for investigating the properties of new crystal materials [32,33].

Sm^{3+}-doped yttrium gallium garnet single crystals were prepared by the optical floating zone method, and their physical and optical properties were compared with those of YAG: Sm^{3+} crystals. These materials were then characterized by XRD, photoluminescence (PL) spectroscopy, and fluorescence lifetime measurements.

2. Materials and Methods

2.1. Crystal Preparation

Nanometer-size powders of Ga_2O_3 (99.99%, Maklin), Sm_2O_3 (99.99%, Aladdin), Y_2O_3 (99.99%, Maklin) and Al_2O_3 (99.99%, Maklin) were purchased in China and used to produce crystals with the empirical composition $Y_{2\cdot96}Sm_{0\cdot04}Ga_5O_{12}$ and $Y_{2\cdot96}Sm_{0\cdot04}Al_5O_{12}$ by the optical floating zone (OFZ) method. A more detailed description of the preparative procedures has been presented in previous work [34–36].

As shown in Figure 1, the prepared samples were light yellow in color and had no cracks or inclusions. Slices were cut and polished on both sides to produce 1.0 mm thick discs for spectroscopic measurements. In addition, crystal fragments were ground in an agate mortar to produce fine powders for X-ray diffraction (XRD) measurements (Dandong Hao Yuan Company, Dandong City, Liaoning Province, China).

2.2. Physical Measurements

Powder samples ground from crystal were measured by XRD (DX-2700, Dandong Hao Yuan Company, Dandong City, Liaoning Province, China) at room temperature using Cu-Kα radiation (λ = 1.54060 nm). Measurements were performed over the range 10–90° 2θ in steps of 0.02° with sampling times of 3 s, and the resulting XRD patterns were analyzed using Jade software (MDI Jade 6.0).

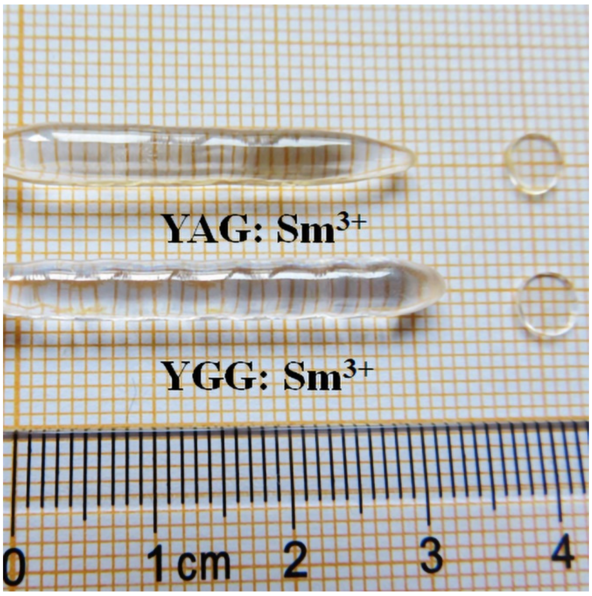

Figure 1. YGG: Sm^{3+} and YAG: Sm^{3+} single crystal rods along with cut and polished crystal slices.

Crystal densities were measured by a high-precision density tester (DE-120M, Daho Meter Company, Dongguan, Guangdong Province, China). By measuring the weight of YGG: Sm^{3+} and YAG: Sm^{3+} single crystal rods in air and pure water, respectively, the volume of the crystal V can be obtained based on the Archimedes principle:

$$V = \frac{M - F}{\rho_w} \quad (1)$$

where M is the weight of the crystal in air (in grams), F is the weight of the crystal in pure water (in grams), and ρ_w is the density of pure water at room temperature, which is 1.0 g/cm^3. The density of the crystal ρ can be calculated by the following formula:

$$\rho = \frac{M}{V} \quad (2)$$

Absorption spectra were obtained in the 250–550 nm range with a UV-Vis Spectrophotometer (UV-2700, Shimadzu, Kyoto, Japan).

A photoluminescence spectrometer (ZLF-325, Zolix Instruments Co., Ltd., Beijing, China) was used to measure the photoluminescence emission (PL) and excitation spectra (PLE), with a 150 W xenon lamp as the excitation light source.

Fluorescence lifetimes were obtained with an Edinburgh steady/transient fluorescence spectrometer (FLS1000, Edinburgh, UK) under excitation with 407 nm light, and then the average lifetime of the samples was determined by tri-exponential fitting.

3. Results and Discussion

3.1. X-ray Diffraction

The XRD patterns of powders ground from YGG: Sm^{3+} and YAG: Sm^{3+} single crystals (Figure 2) are consistent with the diffraction peaks of the YGG standard card (PDF c-01-071-2151) and YAG standard card (PDF c-01-088-2048), respectively. The diffraction peaks for both samples are narrow and demonstrate that the crystals have a good crystallinity. One can also see in Figure 2 that the YGG: Sm^{3+} crystal peaks are shifted to lower angles compared to the YAG: Sm^{3+} samples, thus confirming that replacing Al^{3+} by Ga^{3+} increases the lattice parameter, as expected from its larger size.

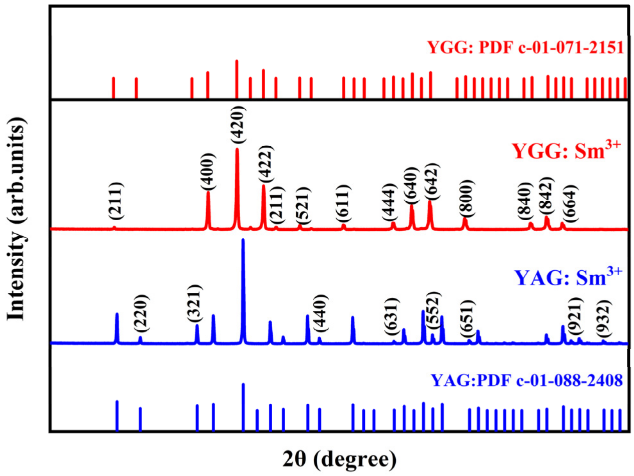

Figure 2. XRD patterns of powders ground from YGG: Sm^{3+} and YAG: Sm^{3+} single crystals.

The cell dimensions and cell volumes of the YGG: Sm^{3+} and YAG: Sm^{3+} crystals calculated using Jade software are shown in Table 1 and demonstrate that the substitution of Ga^{3+} (ionic radius 0.61 Å) for Al^{3+} (ionic radius 0.53 Å) [37] results in an increase in the lattice constant from 1.201 nm to 1.230 nm and in the cell volume from 1.732 nm^3 to 1.860 nm^3.

Table 1. Lattice constants and cell volumes for YGG: Sm^{3+} and YAG: Sm^{3+} crystals.

Sample	Lattice Constant (nm) a = b = c	Cell Volume (nm^3)
YGG: Sm^{3+}	1.230	1.860
YAG: Sm^{3+}	1.201	1.732

3.2. Density Measurement

The measured densities of the YGG: Sm^{3+} and YAG: Sm^{3+} single crystals are shown in Table 2, where *M* is the weight of the crystal in air and *V* is the volume of the crystal. The densities of $Y_{2\cdot96}Sm_{0\cdot04}Ga_5O_{12}$ and $Y_{2\cdot96}Sm_{0\cdot04}Al_5O_{12}$ crystals obtained from the present work (ρ) are 5.756 and 4.533 g/cm^3, respectively, which are very close to the densities of crystals calculated by Jade (ρ_{cal} in Table 2), indicating that our experimental data are effective and reliable. The density of YGG: Sm^{3+} crystal is higher than that of YAG: Sm^{3+} crystal because the atomic mass of Ga (69.72) is greater than that of Al (26.98).

Table 2. The densities of $Y_{2\cdot96}Sm_{0\cdot04}Ga_5O_{12}$ and $Y_{2\cdot96}Sm_{0\cdot04}Al_5O_{12}$ single crystals.

Crystal	*M* (g)	*V* (cm^3)	ρ (g/cm^3)	ρ_{cal} (g/cm^3)
$Y_{2\cdot96}Sm_{0\cdot04}Ga_5O_{12}$	2.498	0.434	5.756	5.765
$Y_{2\cdot96}Sm_{0\cdot04}Al_5O_{12}$	2.561	0.565	4.533	4.551

3.3. Absorption Spectra

Figure 3a shows the absorption spectra of YGG: Sm^{3+} and YAG: Sm^{3+} crystals, and Figure 3b shows the optical band gaps of YGG: Sm^{3+} and YAG: Sm^{3+} crystals. The absorption spectra of YGG: Sm^{3+} and YAG: Sm^{3+} single crystals in the range of 250 nm to 550 nm (Figure 3a) are similar because they are derived from transitions between Sm^{3+} 4*f* electronic energy levels, which are largely shielded from external structural effects. Ten absorption peaks were observed at 345, 362, 377, 390, 407, 419, 439, 468, 482 and 495 nm, corresponding to $^6H_{5/2} \rightarrow {}^4D_{7/2}$, $^4D_{3/2}$, $^6P_{7/2}$, $^4L_{15/2}$, $^4F_{7/2}$, $^6P_{5/2}$, $^4G_{9/2}$, $^4I_{13/2}$, $^4I_{9/2}$ and $^4G_{7/2}$ transitions, respectively [38]. The transition $^6H_{5/2} \rightarrow {}^4F_{7/2}$ (407 nm) appears to be stronger than other transitions and is more intense in the YGG: Sm^{3+} crystal than in the YAG: Sm^{3+} crystal, thus demonstrating that crystal density and differences in the ionic radii of Al^{3+} and Ga^{3+} in YAG and YGG can affect the intensity of the Sm^{3+} electronic absorption transitions. Moreover, the absorptions at 407 and 468 nm indicate that YGG: Sm^{3+} crystals can be excited by InGaN-based light-emitting diodes and are thus fluorescent materials for manufacturing white LEDs [39]. The absorption peak in the range of 250 nm to 330 nm (Figure 3a) corresponds to the absorption of the matrix, and the absorption edge of YGG: Sm^{3+} single crystal shifts to a longer wavelength than YAG: Sm^{3+} single crystal, which is because YGG and YAG crystals are different substrates and have different band gaps [40].

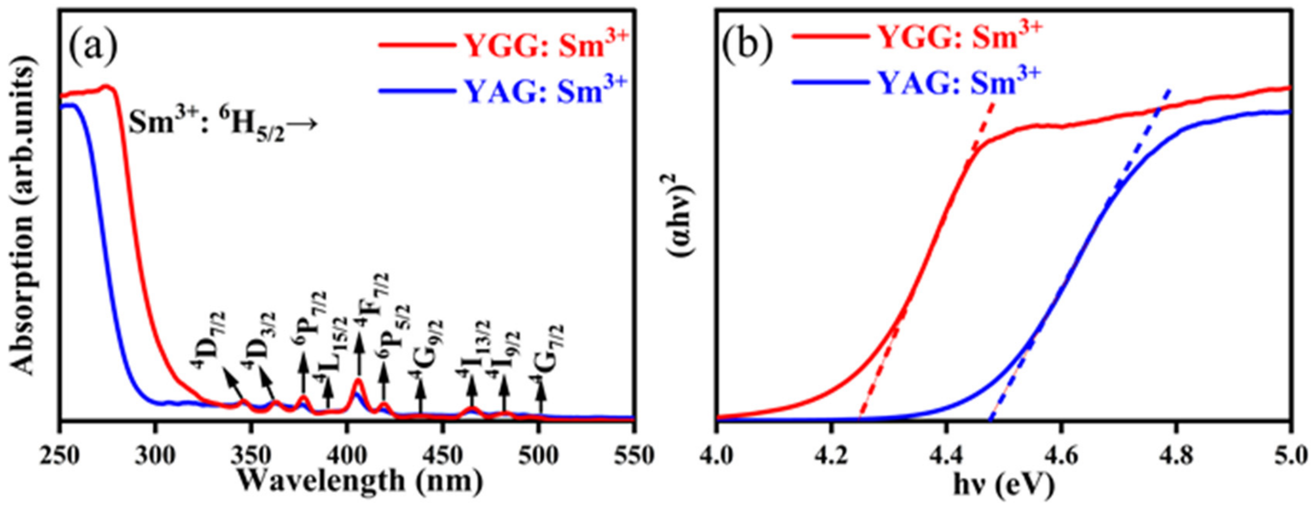

Figure 3. (**a**) UV-Vis absorption spectra of YGG: Sm^{3+} and YAG: Sm^{3+} single crystals; (**b**) determination of E_g (the optical band gap) in YGG: Sm^{3+} and YAG: Sm^{3+} single crystals.

The optical band gaps (E_g) of the YGG: Sm^{3+} and YAG: Sm^{3+} single crystals were determined from the position of the charge transfer transition using the Tauc equation [41]:

$$(\alpha h v)^2 = A(hv - E_g) \tag{3}$$

where α and hv are the absorption coefficients and phonon energy of the sample, respectively, and A is a constant. The relationship $(\alpha hv)^2$ versus hv is indicated in Figure 3b, and E_g is the position of the intersection of the linear part of the curve with the hv axis. The optical band gaps in YGG: Sm^{3+} and YAG: Sm^{3+} single crystals are 4.25 and 4.47 eV, respectively, showing that YGG: Sm^{3+} single crystal has a narrower optical band gap than YAG: Sm^{3+} single crystal.

3.4. Luminescence Properties

3.4.1. PLE Spectrum

The photoluminescence excitation (PLE) spectra detected at 613 nm for YGG: Sm^{3+} and YAG: Sm^{3+} single crystals are shown in Figure 4. The peaks at 336 nm, 348 nm, 365 nm, 379 nm, 407 nm, 420 nm, 440 nm, 468 nm, 482 nm, 493 nm, and 543 nm correspond to transitions from the Sm^{3+} $^6H_{5/2}$ ground state to the $^4P_{3/2}$, $^4D_{7/2}$, $^4D_{3/2}$, $^6P_{7/2}$, $^4F_{7/2}$, $^6P_{5/2}$, $^4G_{9/2}$, $^4I_{13/2}$, $^4I_{9/2}$, $^4G_{7/2}$, and $^4F_{3/2}$ excited states, respectively [18]. The excitation peaks of the YGG: Sm^{3+} crystal at 407 nm and 468 nm are strong; thus, these two wavelengths of light are selected to excite this crystal to study the PL spectrum.

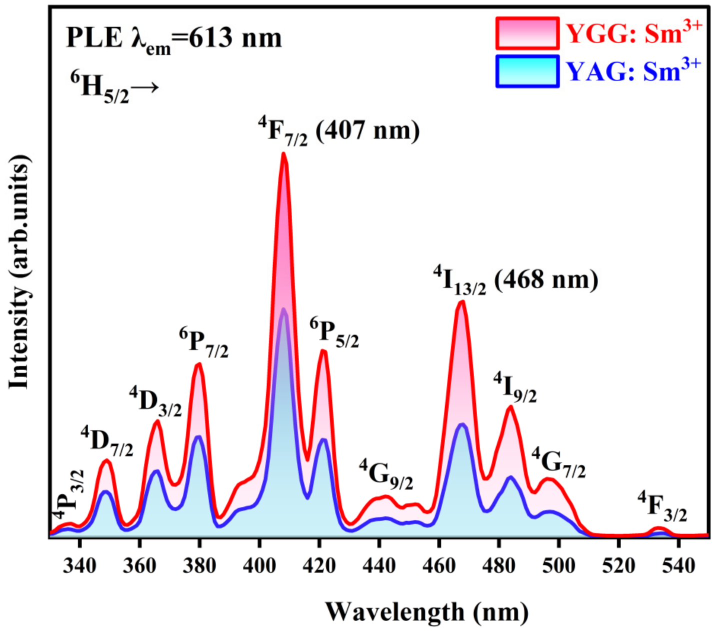

Figure 4. Photoluminescence excitation (PLE) spectra detected at 613 nm for YGG: Sm^{3+} and YAG: Sm^{3+} single crystals.

3.4.2. PL Spectrum

Photoluminescence (PL) spectra of YGG: Sm^{3+} and YAG: Sm^{3+} crystals under excitation at 407 nm and 468 nm are shown in Figures 5 and 6, respectively, and consist of three strong bands and one weak band with centers at about 572 nm, 611 nm, 654 nm and 696 nm corresponding to the Sm^{3+} $^4G_{5/2} \rightarrow {}^6H_j$ (j = 5/2, 7/2, 9/2, 11/2) transitions, respectively [18]. Intensities are in the order $^6H_{7/2} > {}^6H_{5/2} > {}^6H_{9/2} > {}^6H_{11/2}$ in both YGG: Sm^{3+} and YAG: Sm^{3+} crystals.

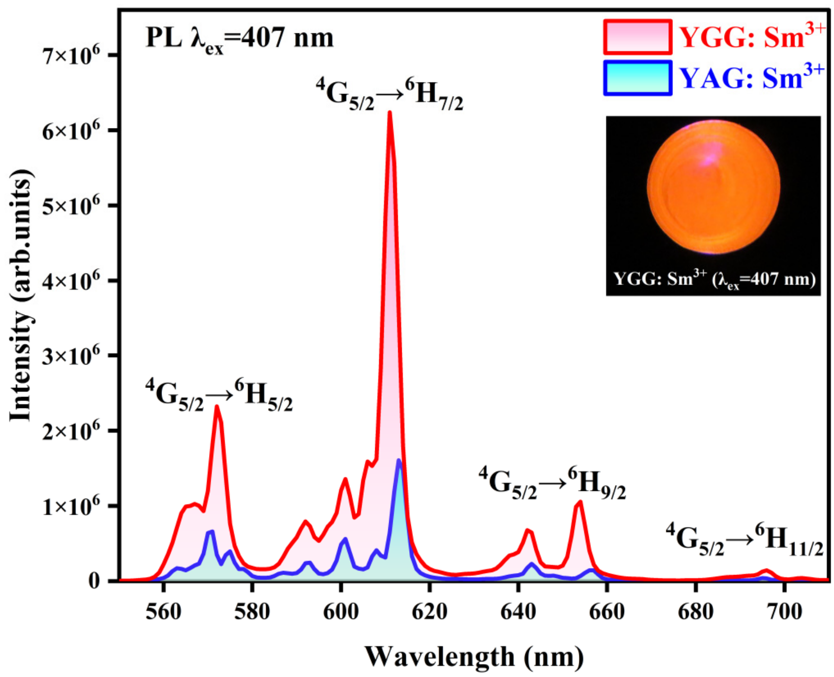

Figure 5. Photoluminescence (PL) spectra of YGG: Sm^{3+} and YAG: Sm^{3+} single crystals under excitation at 407 nm.

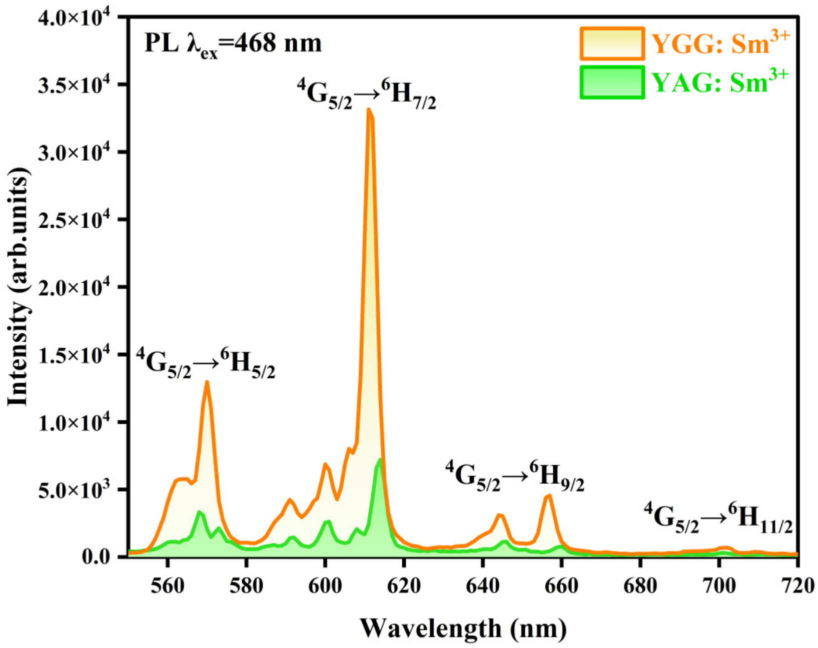

Figure 6. Photoluminescence (PL) spectra of YGG: Sm^{3+} and YAG: Sm^{3+} single crystals under excitation at 468 nm.

Under excitation at 407 nm, the YGG: Sm^{3+} crystal emits bright orange-red light, as shown in Figure 5, and the intensity of YGG: Sm^{3+} crystal is obviously higher than that of YAG: Sm^{3+} crystal. Additionally, the emission spectrum of YGG: Sm^{3+} is blue-shifted relative to the YAG: Sm^{3+} crystal, with maxima at 611 and 613 nm, and the FWHM are 4.1 and 3.8 nm, respectively.

Under excitation at 468 nm (Figure 6), the YGG: Sm^{3+} crystal also emits orange-red light but is two orders of magnitude weaker than under excitation at 407 nm. Furthermore, the luminescence intensity of YGG: Sm^{3+} crystal is higher than that of YAG: Sm^{3+}, and the emission spectrum of YGG: Sm^{3+} is blue-shifted relative to the YAG: Sm^{3+} crystal, with maxima at 611 and 613 nm and FWHM of 4.2 nm.

These results may be a consequence of changing Al^{3+} in the YAG lattice to Ga^{3+}, and Ga^{3+} has a greater atomic mass than Al^{3+} and results in the YGG: Sm^{3+} crystal having a higher density (Table 2) and smaller phonon energy than YAG: Sm^{3+} [42]. The phonon energy directly affects the luminescence efficiency [23]; as a consequence, the emission peak of the YGG: Sm^{3+} crystal is much stronger than that of the YAG: Sm^{3+}. In addition, the crystal fields of YGG and YAG crystals are different, which affects the 4f energy level position and linewidth of Sm^{3+} [43], resulting in a shorter emission wavelength and a blue shift of YGG: Sm^{3+} emission spectra compared with YAG: Sm^{3+} crystals. Thus, YGG represents an improvement over YAG as a crystal matrix for observing the luminescence of rare-earth ions, and at the same time, the YGG: Sm^{3+} crystal has a highly efficient orange-red emission (as shown in Figure 5) and has a potential use in w-LEDs and as orange-red solid-state lasers.

3.5. Chromaticity Coordinates

The luminescence color and color purity are important parameters for evaluating the quality and potential uses of luminescent materials [22,44]. CIE-1931 [45] was used to calculate the chromaticity coordinates for the emission spectra of YGG: Sm^{3+} and YAG: Sm^{3+} single crystals under excitation at 407 nm. As shown in Figure 7 and Table 3, the color coordinates for the spectra from both crystals are located in the orange-red light region, and their color purity was calculated by the following formula [46,47]:

$$\text{color purity} = \frac{\sqrt{(x_s - x_i)^2 + (y_s - y_i)^2}}{\sqrt{(x_d - x_i)^2 + (y_d - y_i)^2}} \times 100\% \quad (4)$$

where (x_s, y_s), (x_i, y_i), and (x_d, y_d) are the color coordinates of the crystals, the color coordinates of isoenergetic white light (0.333, 0.333), and the color coordinates of the main peak of the emission spectrum, respectively. As shown in Table 3, under excitation at 407 nm, the color purity is around 85% for the YGG: Sm^{3+} crystal and around 83% for YAG: Sm^{3+}. Thus, YGG: Sm^{3+} single crystals are high-quality materials that emit orange-red light, with notable improvements in efficiency over YAG: Sm^{3+}.

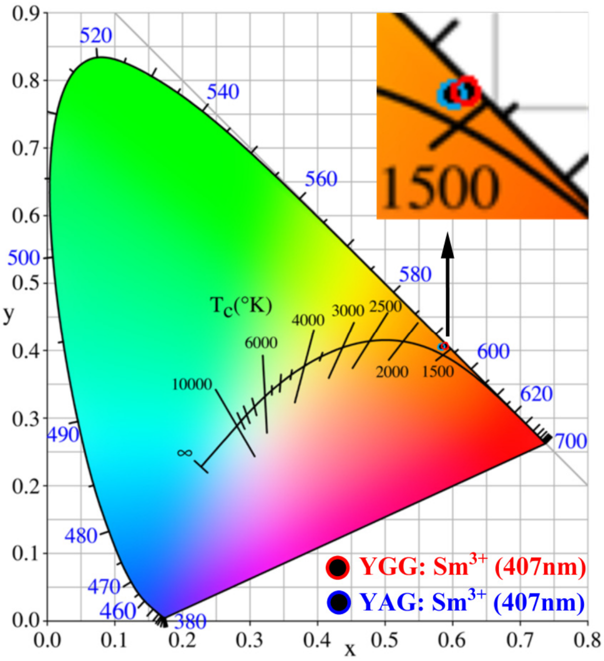

Figure 7. Chromaticity diagram for YGG: Sm^{3+} crystal and YAG: Sm^{3+} crystal with their positions shown in expanded form in the insert.

Table 3. Values of CIE coordinates (x_s, y_s) and color purities calculated for YGG: Sm^{3+} and YAG: Sm^{3+} crystals.

Sample	λex (nm)	(x_s, y_s)	(x_d, y_d)	Color Purity
YGG: Sm^{3+}	407	(0.590, 0.407)	(0.646, 0.354)	85%
YAG: Sm^{3+}	407	(0.584, 0.405)	(0.647, 0.353)	83%

3.6. Fluorescence Lifetime Measurements

The fluorescence lifetime ($\overline{\tau}$) is defined as the time required after ceasing excitation for the fluorescence intensity to drop to 1/e of its maximum [48]. The fluorescence decay curves (Figure 8) for the Sm^{3+} $^4G_{5/2} \rightarrow {}^6H_{7/2}$ transition in YGG: Sm^{3+} and YAG: Sm^{3+} crystals under excitation at 407 nm are similar and were fitted with a three-exponential function [49]:

$$I(t) = A_1 e^{(-t/\tau_1)} + A_2 e^{(-t/\tau_2)} + A_3 e^{(-t/\tau_3)} \quad (5)$$

where $I(t)$ is the luminescence intensity as a function of time t, and A_1, A_2, and A_3 are the pre-exponential factors of the three lifetimes τ_1, τ_2 and τ_3 (Table 4) [49]. This indicates that there are three decay behaviors. The first component (τ_1) is dominant and could be attributed to the Sm^{3+} ions [50]. The second (τ_2) and third (τ_3) components are longer than the first component (τ_1); therefore, τ_2 and τ_3 could be related to the flicker light emitted by excitons associated with antisite defects in the matrix [51]. The average decay time of the sample is then defined by (6) [49]:

$$\overline{\tau} = \frac{A_1\tau_1^2 + A_2\tau_2^2 + A_3\tau_3^2}{A_1\tau_1 + A_2\tau_2 + A_3\tau_3} \tag{6}$$

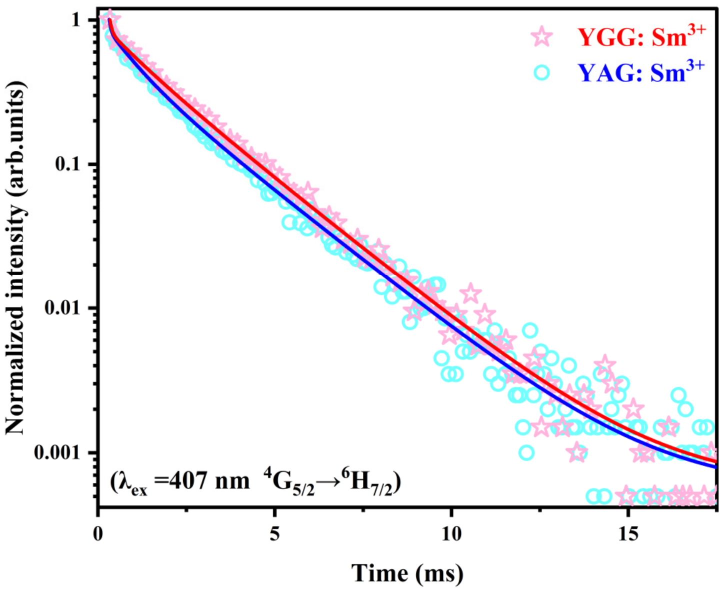

Figure 8. Fluorescence decay curves for the YGG: Sm^{3+} and YAG: Sm^{3+} single crystals.

Table 4. Pre-exponential factors (A) and individual lifetimes (τ) for YGG: Sm^{3+} and YAG: Sm^{3+} single crystals.

Crystal	A_1	τ_1	A_2	τ_2	A_3	τ_3	$\overline{\tau}$	R^2
YGG: Sm^{3+}	69.89	0.06	0.24	0.95	0.76	2.21	0.705	0.998
YAG: Sm^{3+}	124.01	0.05	0.46	0.78	0.61	2.24	0.466	0.998

The fluorescence lifetimes for the $^4G_{5/2} \rightarrow {}^6H_{7/2}$ emission peak from YGG: Sm^{3+} and YAG: Sm^{3+} single crystals were then calculated to be 0.705 ms and 0.466 ms, respectively (Table 4). Thus, the fluorescence lifetime of YGG: Sm^{3+} is not only longer than that of the YAG: Sm^{3+} crystal, but it is also longer than those of $CaGdAlO_4$: Sm^{3+} (0.69 ms) and $NaGd(MnO_4)$: Sm^{3+} crystals (0.5574 ms) [18,52,53]; this is probably the consequence of the greater intensity of its $^4G_{5/2} \rightarrow {}^6H_{7/2}$ emission peak, which allows for a greater participation of Sm^{3+} ions in this transition and results in a longer fluorescence lifetime [54,55].

4. Conclusions

High-quality $Y_{2\cdot96}Sm_{0\cdot04}Ga_5O_{12}$ (YGG: Sm^{3+}) single crystals were successfully prepared for the first time by the optical floating zone method and were compared with $Y_{2\cdot96}Sm_{0\cdot04}Al_5O_{12}$ (YAG: Sm^{3+}) single crystals. The density of $Y_{2\cdot96}Sm_{0\cdot04}Ga_5O_{12}$ single crystal (5.756 g/cm^3) is larger than that of $Y_{2\cdot96}Sm_{0\cdot04}Al_5O_{12}$ single crystal (4.481 g/cm^3), because of the larger atomic mass of Ga compared with Al. XRD analysis showed that Sm^{3+} successfully entered into the cubic-phase structure of the garnet crystals. Ten absorption peaks were observed at 345, 362, 377, 390, 407, 419, 439, 468, 482 and 495 nm, corresponding to $^6H_{5/2} \rightarrow {}^4D_{7/2}$, $^4D_{3/2}$, $^6P_{7/2}$, $^4L_{15/2}$, $^4F_{7/2}$, $^6P_{5/2}$, $^4G_{9/2}$, $^4I_{13/2}$, $^4I_{9/2}$ and $^4G_{7/2}$ transitions of Sm^{3+}, respectively. Excitation peaks at similar wavelengths were observed in the PLE spectra detected at 613 nm, including strong peaks at 407 nm and 468 nm. Both YGG:

Sm^{3+} and YAG: Sm^{3+} crystals emit orange-red light with a wavelength of about 611 nm under excitation at 407 and 468 nm, respectively, and the luminescence intensity is much stronger with 407 nm excitation. Furthermore, with both PL spectra, the emission peaks from YGG: Sm^{3+} crystal are both significantly more intense than those from YAG: Sm^{3+}, and both experience a blue shift. The YGG: Sm^{3+} crystal has a highly efficient orange-red emission. In addition, under the excitation of 407 nm, the color purity of the orange-red light emitted by the YGG: Sm^{3+} crystal (85%) is higher than that emitted by the YAG: Sm^{3+} crystal (83%). Additionally, the fluorescence lifetime at the $^4G_{5/2} \rightarrow {}^6H_{7/2}$ transition of the YGG: Sm^{3+} crystal (0.705 ms) is longer than that of the YAG: Sm^{3+} crystal (0.466 ms). This shows that the optical properties of YGG: Sm^{3+} crystal are better than those of YAG: Sm^{3+} crystal and that they have a potential use in w-LEDs and as orange-red solid-state lasers. In other words, YGG: Sm^{3+} crystals are promising new materials for use in w-LEDs and orange-red solid-state lasers.

Author Contributions: Conceptualization, H.Z.; methodology, H.Z.; software, H.Z., Z.Z. and S.T.; validation, H.Z., S.X. and W.D.; formal analysis, H.Z., N.Z. and L.W.; investigation, H.Z. and W.W.; resources, W.D.; data curation, H.Z., Z.Z. and P.Z.; writing—original draft preparation, H.Z.; writing—review and editing, H.Z., B.A.G. and W.D.; visualization, B.A.G., W.D. and S.X.; supervision, S.X. and W.D.; project administration W.D.; funding acquisition, W.D.; All authors have read and agreed to the published version of the manuscript.

Funding: This work was supported by the National Natural Science Foundations of China under Grant Nos. 12175047 and 11975004, and the Science and Technology Foundation of Guangxi University, China under Grant No. 2023BZXM003.

Data Availability Statement: The data presented in this study are available on reasonable request from the corresponding author.

Acknowledgments: The authors gratefully thank Dingkang Xiong and Yuyang Huang for useful discussions on the subject matter of this paper.

Conflicts of Interest: The authors declare no conflict of interest.

References

1. Wang, Y.; Zhu, Z.; Ta, S.; Cheng, Z.; Zhang, P.; Zeng, N.; Goodman, B.A.; Xu, S.; Deng, W. Optical Properties of Yttria-Stabilized Zirconia Single-Crystals Doped with Terbium Oxide. *Crystals* **2022**, *12*, 1081. [CrossRef]
2. Yu, Z.; Zhang, C.; Lou, X.; Zuo, R.; Yang, Y.; Jia, G. Rare earth ions doped Bi_2MoO_6 luminescent materials: Pechini sol-gel synthesis, down-conversion and up-conversion multicolor emissions, and potential applications. *Ceram. Int.* **2023**, *49*, 25987–25997. [CrossRef]
3. Jamalaiah, B.C.; Rasool, S.N. Luminescence properties of $GdAl_3(BO_3)_4$: Dy^{3+} phosphors for white-LEDs. *Mater. Today* **2016**, *3*, 4019–4022. [CrossRef]
4. Kumar, V.; Som, S.; Dutta, S.; Das, S.; Swart, H.C. Influence of Ho^{3+} doping on the temperature sensing behavior of Er^{3+}–Yb^{3+} doped La_2CaZnO_5 phosphor. *RSC Adv.* **2016**, *6*, 84914–84925. [CrossRef]
5. Chen, Y.F.; Tsai, S.W. Diode-pumped Q-switched Nd: YVO_4 yellow laser with intracavity sum-frequency mixing. *Opt. Lett.* **2002**, *27*, 397–399. [CrossRef] [PubMed]
6. Yang, Y.; Xu, S.; Li, S.; Wu, W.; Pan, Y.; Wang, D.; Hong, X.; Cheng, Z.; Deng, W. Luminescence Properties of Ho_2O_3-Doped Y_2O_3 Stabilized ZrO_2 Single Crystals. *Crystals* **2022**, *12*, 415. [CrossRef]
7. Yousif, A.; Abbas, B.H.; Vijay, K.; Anurag, P.; Swart, H.C. Luminescence properties of Eu^{3+} activated Y_2O_3 red phosphor with incorporation of Ga^{3+} and Bi^{3+} trace hertero-cations in the Y_2O_3 lattice. *Vacuum* **2018**, *155*, 73–75. [CrossRef]
8. Pandey, A.; Kumar, V.; Som, S.; Yousif, A.; Kroon, R.E.; Coetsee, E.; Swart, H.C. Photon and electron beam pumped luminescence of Ho^{3+} activated $CaMoO_4$ phosphor. *Appl. Surf. Sci.* **2017**, *423*, 1169–1175. [CrossRef]
9. Liu, R.; Wang, D.; Chen, M.; Liu, L.; Zhou, Y.; Zeng, F.; Su, Z. Luminescence, energy transfer properties of Dy^{3+}/Eu^{3+} coactivated neutral and warm white emissions GSBG glasses. *J. Lumin.* **2021**, *237*, 118180. [CrossRef]
10. Çelik Gül, G.; Kurtuluş, F. RE (Y, Er, Gd, La, Nd, Sm, Dy)-doped $SrBPO_5$ colorful phosphors: Definition of structural unit cell parameters and optical properties. *Optik* **2017**, *139*, 265–271. [CrossRef]
11. Pandey, A.; Kumar, V.; Kroon, R.E.; Swart, H.C. Temperature induced upconversion behaviour of Ho^{3+}-Yb^{3+} codoped yttrium oxide films prepared by pulsed laser deposition. *J. Alloys Compd.* **2016**, *672*, 190–196. [CrossRef]
12. Gao, T.; Tian, J.; Liu, Y.; Liu, R.; Zhuang, W. Garnet phosphors for white-light-emitting diodes: Modification and calculation. *Dalton Trans.* **2021**, *50*, 3769–3781. [CrossRef] [PubMed]

13. Hu, S.; Lu, C.; Zhou, G.; Liu, X.; Qin, X.; Liu, G.; Wang, S.; Xu, Z. Transparent YAG:Ce ceramics for WLEDs with high CRI: Ce^{3+} concentration and sample thickness effects. *Ceram. Int.* **2016**, *42*, 6935–6941. [CrossRef]
14. Du, Q.; Feng, S.; Qin, H.; Hua, H.; Ding, H.; Jia, L.; Zhang, Z.; Jiang, J.; Jiang, H. Massive red-shifting of Ce^{3+} emission by Mg^{2+} and Si^{4+} doping of YAG: Ce transparent ceramic phosphors. *J. Mater. Chem. C* **2018**, *6*, 12200–12205. [CrossRef]
15. Gu, C.; Wang, X.-J.; Xia, C.; Li, S.; Liu, P.; Li, D.; Li, H.; Zhou, G.; Zhang, J.; Xie, R.-J. A new CaF_2-YAG: Ce composite phosphor ceramic for high-power and high-color-rendering WLEDs. *J. Mater. Chem. C* **2019**, *7*, 8569–8574. [CrossRef]
16. Yao, Q.; Hu, P.; Sun, P.; Liu, M.; Dong, R.; Chao, K.; Liu, Y.; Jiang, J.; Jiang, H. YAG: Ce^{3+} transparent ceramic phosphors brighten the next-generation laser-driven lighting. *Adv. Mater.* **2020**, *32*, 1907888. [CrossRef] [PubMed]
17. Zhang, J.F.; Gu, G.R.; Di, X.X.; Xiang, W.D.; Liang, X.J. Optical characteristics of Ce, Eu: YAG single crystal grown by Czochralski method. *J. Rare Earths* **2019**, *37*, 145–150. [CrossRef]
18. Tan, X.; Xu, S.; Wang, X.; Liu, F.; Goodman, B.A.; Xiong, D.; Deng, W. Preparation and optical properties of samaria-doped yttria-stabilized zirconia single crystals. *J. Am. Ceram. Soc.* **2019**, *102*, 6863–6871. [CrossRef]
19. Gu, G.; Xiang, W.; Yang, C.; Liang, X. Synthesis and luminescence properties of a H_2 annealed Mn-doped $Y_3Al_5O_{12}$: Ce^{3+} single crystal for WLEDs. *CrystEngComm* **2015**, *17*, 4554–4561. [CrossRef]
20. Demesh, M.; Dernovich, O.; Gusakova, N.; Yasukevich, A.; Kornienko, A.; Dunina, E.; Fomicheva, L.; Pavlyuk, A.; Kuleshov, N. Growth and spectroscopic properties of Sm^{3+}: $KY(WO_4)_2$ crystal. *Opt. Mater.* **2018**, *75*, 821–826. [CrossRef]
21. Rezende, M.V.d.S.; Paschoal, C.W.A. Radioluminescence enhancement in Eu^{3+}-doped $Y_3Al_5O_{12}$ phosphors by Ga substitution. *Opt. Mater.* **2015**, *46*, 530–535. [CrossRef]
22. Yousif, A.; Som, S.; Kumar, V.; Swart, H. Comparison and analysis of Eu^{3+} luminescence in $Y_3Al_5O_{12}$ and $Y_3Ga_5O_{12}$ hosts material for red lighting phosphor. *Mater. Chem. Phys.* **2015**, *166*, 167–175. [CrossRef]
23. You, L.; Zhao, Y.; Lu, D.; Liang, F.; Li, L.; Chen, Y.; Liu, J.; Wang, J.; Yu, H.; Zhang, H. High-efficiency Er-doped yttrium gallium garnet laser resonantly pumped by a laser diode at 1.47 µm. *Opt. Lett.* **2020**, *45*, 4361–4364. [CrossRef] [PubMed]
24. Zeng, W.; Xia, F.; Tian, W.; Cao, F.; Chen, J.; Wu, J.; Song, R.; Mu, S. Single-crystal high-nickel layered cathodes for lithium-ion batteries: Advantages, mechanism, challenges and approaches. *Curr. Opin. Electrochem.* **2022**, *31*, 100831. [CrossRef]
25. Lou, Y.; Zhang, S.; Gu, Z.; Wang, N.; Wang, S.; Zhang, Y.; Song, Y. Perovskite single crystals: Dimensional control, optoelectronic properties, and applications. *Mater. Today* **2023**, *62*, 225–250. [CrossRef]
26. Kataoka, K.; Akimoto, J. Lithium-ion conductivity and crystal structure of garnet-type solid electrolyte $Li_{7-x}La_3Zr_{2-x}Ta_xO_{12}$ using single-crystal. *J. Ceram. Soc.* **2019**, *127*, 521–526. [CrossRef]
27. Han, Z.; Sun, D.; Zhang, H.; Luo, J.; Quan, C.; Hu, L.; Dong, K.; Cheng, M.; Chen, G.; Hang, Y. Investigation on the growth and properties of six garnet single crystals with large lattice constants. *Cryst. Res. Technol.* **2021**, *56*, 2000221. [CrossRef]
28. Hong, X.; Zhang, L.; Xu, S.; Cheng, Z.; Wang, Y.; Goodman, B.A.; Xiong, D.; Deng, W. White light luminescence in Dy/Tm co-doped yttria stabilized zirconia single crystals. *J. Rare Earths* **2022**. [CrossRef]
29. Koohpayeh, S.M.; Fort, D.; Abell, J.S. The optical floating zone technique: A review of experimental procedures with special reference to oxides. *Prog. Cryst. Growth Charact. Mater.* **2008**, *54*, 121–137. [CrossRef]
30. Li, S.; Xu, S.; Wang, X.; Wang, D.; Goodman, B.A.; Hong, X.; Deng, W. Optical properties of gadolinia-doped cubic yttria stabilized zirconia single crystals. *Ceram. Int.* **2021**, *47*, 3346–3353. [CrossRef]
31. Wolff, N.; Schwaigert, T.; Siche, D.; Schlom, D.G.; Klimm, D. Growth of $CuFeO_2$ single crystals by the optical floating-zone technique. *J. Cryst. Growth* **2020**, *532*, 125426. [CrossRef]
32. Xu, B.; Yang, X.; Cheng, H.; Zhao, J.; Wang, Y.; Zhu, E.; Zhang, J. Preparation, characterization and property of high-quality LaB_6 single crystal grown by the optical floating zone melting technique. *Vacuum* **2019**, *168*, 108845. [CrossRef]
33. Tang, H.; Zhang, X.; Cheng, L.; Xie, J.; Yu, X.; Mi, X.; Liu, Q. Broadband emission of $Lu_3Mg_2GaSi_2O_{12}$: Ce^{3+}, Sm^{3+} phosphors and their potential application for w-LEDs. *Ceram. Int.* **2021**, *47*, 26410–26420. [CrossRef]
34. Wu, T.; Wang, L.; Shi, Y.; Xu, T.; Wang, H.; Fang, J.; Ni, J.; He, H.; Wang, C.; Wan, B.; et al. Fast $(Ce,Gd)_3Ga_2Al_3O_{12}$ Scintillators Grown by the Optical Floating Zone Method. *Cryst. Growth Des.* **2022**, *22*, 180–190. [CrossRef]
35. Xu, S.; Tan, X.; Liu, F.; Zhang, L.; Huang, Y.; Goodman, B.A.; Deng, W. Growth and optical properties of thulia-doped cubic yttria stabilized zirconia single crystals. *Ceram. Int.* **2019**, *45*, 15974–15979. [CrossRef]
36. Wu, W.; Wang, D.; Pan, Y.; Yang, Y.; Zhang, P.; Xu, S.; Goodman, B.A.; Deng, W. Characterization of interactive up-conversion luminescence mechanisms in $Tm^{3+}/Ho^{3+}/Yb^{3+}$ doped yttria stabilized zirconia single crystals. *Opt. Mater.* **2022**, *123*, 111827. [CrossRef]
37. Shannon, R.D. Revised effective ionic radii and systematic studies of interatomic distances in halides and chalcogenides. *Acta Crystallogr. A* **1976**, *32*, 751–767. [CrossRef]
38. Brito, D.R.N.; Queiroz, M.N.; Barboza, M.J.; Steimacher, A.; Pedrochi, F. Investigation of optical and spectroscopic properties of Sm^{3+} ions in CaBAl glasses. *Opt. Mater.* **2017**, *64*, 114–120. [CrossRef]
39. Liu, W.; Zhang, Q.; Sun, D.; Luo, J.; Gu, C.; Jiang, H.; Yin, S. Crystal growth and spectral properties of Sm: GGG crystal. *J. Cryst. Growth* **2011**, *331*, 83–86. [CrossRef]
40. Jubu, P.R.; Yam, F.K.; Chahrour, K.M. Enhanced red shift in optical absorption edge and photoelectrochemical performance of N-incorporated gallium oxide nanostructures. *Vacuum* **2020**, *182*, 109704. [CrossRef]
41. Makuła, P.; Pacia, M.; Macyk, W. How To Correctly Determine the Band Gap Energy of Modified Semiconductor Photocatalysts Based on UV–Vis Spectra. *J. Phys. Chem. Lett.* **2018**, *9*, 6814–6817. [CrossRef] [PubMed]

42. Kittel, C. *Introduction to Solid State Physics*; John Wiley & Sons, Inc: Hoboken, NJ, USA, 2005.
43. Pirri, A.; Maksimov, R.N.; Shitov, V.A.; Osipov, V.V.; Sani, E.; Patrizi, B.; Vannini, M.; Toci, G. Continuously tuned $(Tm_{0.05}Sc_{0.252}Y_{0.698})_2O_3$ ceramic laser with emission peak at 2076 nm. *J. Alloys Compd.* **2021**, *889*, 161585. [CrossRef]
44. Han, L.; Hu, Y.; Pan, M.; Xie, Y.; Liu, Y.; Li, D.; Dong, X. A new tactic to achieve Y_2O_2S: Yb^{3+}/Er^{3+} up-conversion luminescent hollow nanofibers. *CrystEngComm* **2015**, *17*, 2529–2535. [CrossRef]
45. Wang, D.; Wu, W.; Tan, X.; Goodman, B.A.; Xu, S.; Deng, W. Upconversion Visible Light Emission in Yb/Pr Co-Doped Yttria-Stabilized Zirconia (YSZ) Single Crystals. *Crystals* **2021**, *11*, 1328. [CrossRef]
46. Wu, G.; Xue, J.; Li, X.; Bi, Q.; Sheng, M.; Leng, Z. A novel red-emitting $Na_5W_3O_9F_5$: Eu^{3+} phosphor with high color purity for blue-based WLEDs. *Ceram. Int.* **2023**, *49*, 10615–10624. [CrossRef]
47. Liu, G.; Zhou, H.; Che, Q.; Liu, B.; Li, J.; Cao, B.; Liu, Z. A novel phosphor of Cu^+-doped PbBrOH: Preparation, luminescence mechanism, and outstanding properties. *J. Mater. Chem. C* **2021**, *9*, 9178–9187. [CrossRef]
48. Naresh, V.; Buddhudu, S. Analysis of energy transfer based emission spectra of (Sm^{3+}, Dy^{3+}): Li_2O–LiF–B_2O_3–CdO glasses. *J. Lumin.* **2014**, *147*, 63–71. [CrossRef]
49. Naresh, V.; Gupta, K.; Parthasaradhi Reddy, C.; Ham, B.S. Energy transfer and colour tunability in UV light induced $Tm^{3+}/Tb^{3+}/Eu^{3+}$: ZnB glasses generating white light emission. *Acta A Mol. Biomol. Spectrosc.* **2017**, *175*, 43–50. [CrossRef]
50. Skaudžius, R.; Enseling, D.; Skapas, M.; Selskis, A.; Pomjakushina, E.; Jüstel, T.; Kareiva, A.; Rüegg, C. Europium–enabled luminescent single crystal and bulk YAG and YGG for optical imaging. *Opt. Mater.* **2016**, *60*, 467–473. [CrossRef]
51. Luque, A.; Martí, A.; Antolín, E.; Tablero, C. Intermediate bands versus levels in non-radiative recombination. *Phys. Rev. B Condens. Matter* **2006**, *382*, 320–327. [CrossRef]
52. Xu, X.; Hu, Z.; Li, R.; Li, D.; Di, J.; Su, L.; Yang, Q.; Sai, Q.; Tang, H.; Wang, Q. Polarized spectral properties of Sm: $CaGdAlO_4$ crystal for reddish-orange laser. *Opt. Mater.* **2017**, *69*, 333–338. [CrossRef]
53. Huang, J.; Huang, J.; Lin, Y.; Gong, X.; Chen, Y.; Luo, Z.; Huang, Y. Spectroscopic properties of Sm^{3+}-doped $NaGd(MoO_4)_2$ crystal for visible laser application. *J. Lumin.* **2017**, *187*, 235–239. [CrossRef]
54. Qiao, Z.; Qin, C.; He, W.; Gong, Y.; Li, B.; Zhang, G.; Chen, R.; Gao, Y.; Xiao, L.; Jia, S. Robust micropatterns on graphene oxide films based on the modification of fluorescence lifetime for multimode optical recording. *Carbon* **2019**, *142*, 224–229. [CrossRef]
55. Green, D.C.; Holden, M.A.; Levenstein, M.A.; Zhang, S.; Johnson, B.R.G.; Gala de Pablo, J.; Ward, A.; Botchway, S.W.; Meldrum, F.C. Controlling the fluorescence and room-temperature phosphorescence behaviour of carbon nanodots with inorganic crystalline nanocomposites. *Nat. Commun.* **2019**, *10*, 206. [CrossRef]